The Astronomical Journal, 168:72 (16pp), 2024 August https://doi.org/10.3847/1538-3881/ad5444

Unveiling MOA-2007-BLG-192: An M Dwarf Hosting a Likely Super-Earth

Sean K. Terry[1,2], Jean-Philippe Beaulieu[3,4], David P. Bennett[1,2], Euan Hamdorf[4], Aparna Bhattacharya[1,2], Viveka Chaudhry[5], Andrew A. Cole[4], Naoki Koshimoto[6], Jay Anderson[7], Etienne Bachelet[8], Joshua W. Blackman[9], Ian A. Bond[10], Jessica R. Lu[11], Jean Baptiste Marquette[3,12], Clément Ranc[3], Natalia E. Rektsini[3,13], Kailash Sahu[7], and Aikaterini Vandorou[1,2]

[1] Department of Astronomy, University of Maryland, College Park, MD 20742, USA; skterry@umd.edu
[2] Code 667, NASA Goddard Space Flight Center, Greenbelt, MD 20771, USA
[3] Sorbonne Université, CNRS, Institut d'Astrophysique de Paris, IAP, F-75014 Paris, France
[4] School of Natural Sciences, University of Tasmania, Private Bag 37 Hobart, TAS 7001, Australia
[5] Sidwell Friends School, Washington, DC 20016, USA
[6] Department of Earth and Space Science, Graduate School of Science, Osaka University, Osaka, 560-0043, Japan
[7] Space Telescope Science Institute, 3700 San Martin Drive, Baltimore, MD 21218, USA
[8] IPAC, Caltech, Pasadena, CA 91125, USA
[9] Physikalisches Institut, Universität Bern, Gesellschaftsstrasse 6, CH-3012 Bern, Switzerland
[10] School of Mathematical and Computational Sciences, Massey University, Auckland 0632, New Zealand
[11] Department of Astronomy, University of California Berkeley, Berkeley, CA 94720, USA
[12] Laboratoire d'Astrophysique de Bordeaux, CNRS, B18N, allée Geoffroy Saint-Hilaire, Pessac, France
[13] School of Natural Sciences, University of Tasmania, Private Bag 37 Hobart, TAS 70001, Australia
Received 2024 March 18; revised 2024 May 25; accepted 2024 June 3; published 2024 July 15

Abstract

We present an analysis of high-angular-resolution images of the microlensing target MOA-2007-BLG-192 using Keck adaptive optics and the Hubble Space Telescope. The planetary host star is robustly detected as it separates from the background source star in nearly all of the Keck and Hubble data. The amplitude and direction of the lens–source separation allows us to break a degeneracy related to the microlensing parallax and source radius crossing time. Thus, we are able to reduce the number of possible binary-lens solutions by a factor of ∼2, demonstrating the power of high-angular-resolution follow-up imaging for events with sparse light-curve coverage. Following Bennett et al., we apply constraints from the high-resolution imaging on the light-curve modeling to find host star and planet masses of $M_{\rm host} = 0.28 \pm 0.04\ M_\odot$ and $m_p = 12.49^{+65.47}_{-8.03}\ M_\oplus$ at a distance from Earth of $D_L = 2.16 \pm 0.30$ kpc. This work illustrates the necessity for the Nancy Grace Roman Galactic Exoplanet Survey to use its own high-resolution imaging to inform light-curve modeling for microlensing planets that the mission discovers.

Unified Astronomy Thesaurus concepts: Exoplanets (498); Gravitational microlensing (672); Adaptive optics (2281); High-resolution microlensing event imaging (2138); Observational astronomy (1145); Astronomy data modeling (1859); HST photometry (756); Astrometry (80)

1. Introduction

Since the early 1990s, surveys of the Galactic bulge have searched for variations in the brightness of background stars (sources) induced by the gravitational field of foreground objects (lenses). The number of lensing events detected has dramatically increased from a few dozen per year in the 1990s (Udalski et al. 1994; Alcock et al. 1996) to thousands per year currently. At present, there are three primary ground-based surveys that contribute to these lensing event detections: the Optical Gravitational Lensing Experiment (OGLE; Udalski et al. 2015), Microlensing Observations in Astrophysics (MOA; Bond et al. 2001), and the Korea Microlensing Telescope Network (KMTNet; Kim et al. 2016). NASA's Nancy Grace Roman Space Telescope (Roman) is scheduled to launch in the next several years and will conduct the Roman Galactic Bulge Time Domain Survey (GBTDS; Gaudi 2022). As part of this bulge survey, the Roman Galactic Exoplanet Survey (RGES) will be the first dedicated space-based gravitational microlensing survey and is expected to detect over 30,000 microlensing events and over 1400 bound exoplanets during its 5 yr survey (Penny et al. 2019). This mission will complement previous large statistical studies of transiting planets from missions like Kepler/TESS and radial velocity (RV) planets from many ground-based RV surveys. The GBTDS is also expected to discover free-floating planets that do not orbit any host star (Johnson et al. 2020; Sumi et al. 2023; S. A. Johnson et al. 2024, in preparation).

As of the time of this writing, microlensing has detected ∼200 planets at distances up to the Galactic bulge.[14] As for most transient phenomena, one limitation of this method for fully characterizing microlensing systems is the cadence at which the photometric data is obtained by the dedicated ground-based surveys. An effective way to increase the sampling for a given microlensing event is to issue a public alert so that observatories around the world can observe ongoing events as a "follow-up" network of telescopes. MOA-2007-BLG-192 was the first planetary microlensing event detected without follow-up observations from other observatories. The initial analysis reported a low-mass planet orbiting a very-low-mass host star or brown dwarf (Bennett et al. 2008). Due to the lack of follow-up network data for this microlensing event, there are significant gaps in the photometric light-curve

[14] https://exoplanetarchive.ipac.caltech.edu/

coverage, which leads to uncertainties in the derived lens system parameters. There are also additional degeneracies in the interpretation of this lens system that arise from the possible planet–star separations and microlensing parallax. The details of these degeneracies are discussed further in Section 2.1.

One way to mitigate some of these degeneracies is by resolving the source and lens independently with high-angular-resolution imaging, e.g., the Hubble Space Telescope (HST), the Keck telescopes, and the Subaru telescope, several years after peak magnification (Bennett et al. 2006, 2007). This high-angular-resolution imaging can enable measurements of the lens–source separation, relative proper motion, and lens flux, which can then be used with mass–luminosity relations (Henry & McCarthy 1993; Henry et al. 1999; Delfosse et al. 2000) to calculate a direct mass for the host.

This current analysis is part of the NASA Keck Key Strategic Mission Support (KSMS) program, "Development of the WFIRST Exoplanet Mass Measurement Method" (Bennett 2018), which is a pathfinder project for the Nancy Grace Roman Space Telescope (formerly known as WFIRST, hereafter Roman; Spergel et al. 2015). For several years now, the KSMS program has measured the masses of many microlensing host stars and their companions (Bhattacharya et al. 2018; Vandorou et al. 2020; Bennett et al. 2020; Blackman et al. 2021; Terry et al. 2021, 2022), all of which are included in one of the most complete statistical studies of the microlensing exoplanet mass-ratio function (Suzuki et al. 2016, 2018). This statistical study shows a break and likely peak in the mass-ratio function for wide-orbit planets at about a Neptune mass, which is at odds with the runaway gas accretion scenario of the leading core-accretion theory of planet formation (Lissauer 1993; Pollack et al. 1996), which predicts a planet desert at sub-Saturn masses (Ida & Lin 2004) for gas giants at wide orbits.

This paper is organized as follows. In Section 2, we present the light-curve reanalysis of MOA-2007-BLG-192 and explain the challenges in the modeling posed by lack of photometric coverage and degeneracies. In Section 3, we describe the high-angular-resolution HST and Keck adaptive optics (AO) observations and analysis. Section 4 details our direct measurement of the lens system flux and lens–source separation in the Keck and HST data, which allows us to reduce the total number of binary-lens solutions. Section 5 describes the newly derived lens system properties from the light-curve modeling that incorporates the high-resolution imaging results. Finally, we discuss the overall results and conclude the paper in Section 6.

2. Prior Studies of the Microlensing Event MOA-2007-BLG-192

2.1. Fitting the Microlensing Light Curve

MOA-2007-BLG-192 (hereafter MB07192), located at R.A. (J2000) = 18:08:03.80, decl. (J2000) = −27:09:00.27 and Galactic coordinates $(l, b) = (4.03°, -3.39°)$ was first alerted by MOA on 2007 May 24. Due to the faintness of the source and poor weather at the MOA telescope, the event was not alerted until the day that the planetary deviation was observed in the light curve.

Figure 1 shows the observed light curve with OGLE (blue) and MOA (red) data as well as the best-fit planetary model by assuming a double-lens, single-source event (2L1S) from our reanalysis of the light-curve modeling. The original light-curve analysis for this event was presented by Bennett et al. (2008, hereafter B08). The only photometric monitoring of the target during magnification was conducted in the OGLE-I and MOA-R bands. Due to the faintness of the source, there is no direct V-band measurement of the target from OGLE or MOA. In order to get a source color estimate, earlier studies used the photometric measurements from these two data sets and converted to $(V-I)$ color following Gould et al. (2010). As apparent in Figure 1, there are significant gaps in the photometric coverage for this event. Due to this incomplete coverage, there are multiple binary-lens solutions with similar mass ratios that can equally explain the deviations in the light curve due to a binary-lens system.

This lack of coverage also resulted in large uncertainties in the measurement of the angular source size and a poorly determined angular Einstein radius, θ_E. However, these various solutions all gave a low-mass planetary system with a mass ratio of $q \sim 2 \times 10^{-4}$, and with quite large errors on the reported q's. Using the constraints from microlensing parallax and the source star size, B08 concluded that the lens system was composed of a $0.06^{+0.028}_{-0.021}\,M_\odot$ object orbited by a $3.3^{+4.9}_{-1.6}\,M_\oplus$ super-Earth. We note at the time of the B08 publication the MOA team was unaware of systematics in their photometry due to chromatic differential refraction effects (Bennett et al. 2012a). This led to an erroneous measurement of microlensing parallax (π_E) reported in their study. Further, the caustic-crossing models presented in B08 contributed to relatively small error bars on the derived planet mass (see Figure 5 in B08). These caustic-crossing models have now been largely ruled out by this study, therefore the planet mass error bars have increased (see Section 5).

2.2. Constraining the Lensing System with Adaptive Optics

Kubas et al. (2012, hereafter K12) obtained two epochs with NACO AO imaging on the Very Large Telescope (VLT) shortly after the peak of the microlensing event when the target was still magnified by a factor of 1.23, as well as 18 months later at baseline. They observed in three bands, J, H, and K_S; this was the first microlensing event for which a fairly large AO data set had been obtained. The AO data were reduced with the Eclipse package (Devillard 1997) and the authors performed point-spread function (PSF) photometry using the Starfinder tool (Diolaiti et al. 2000). The absolute calibration was performed by a two-stage process using the Two Micron All Sky Survey (2MASS) and data collected by the IRSF telescope in South Africa. Knowing the source flux from the microlensing fit, NACO AO detected excess flux in all three near-IR bands. Assuming that all the excess flux comes from the microlensing images and the lens brightness, they obtained new constraints on the lensing system. Combining the results of the two epochs, they derived that the lens has the following magnitudes: $J_L = 20.73 \pm 0.32$, $H_L = 19.94 \pm 0.35$, and $K_L = 19.16 \pm 0.20$. Using these constraints, and the (erroneous) microlensing parallax fit by B08, they concluded that the lensing system is a $0.084^{+0.015}_{-0.012} M_\odot$ M dwarf at a distance of 660^{+100}_{-70} pc orbited by a $3.2^{+5.2}_{-1.8}\,M_\oplus$ super-Earth at $0.66^{+0.51}_{-0.22}$ au.

2.3. Why Revisit This System?

MB07192 is an important event from the Suzuki et al. (2016) sample of cold planets. Its mass ratio is in the region where a change of slope has been observed in the mass-ratio function.

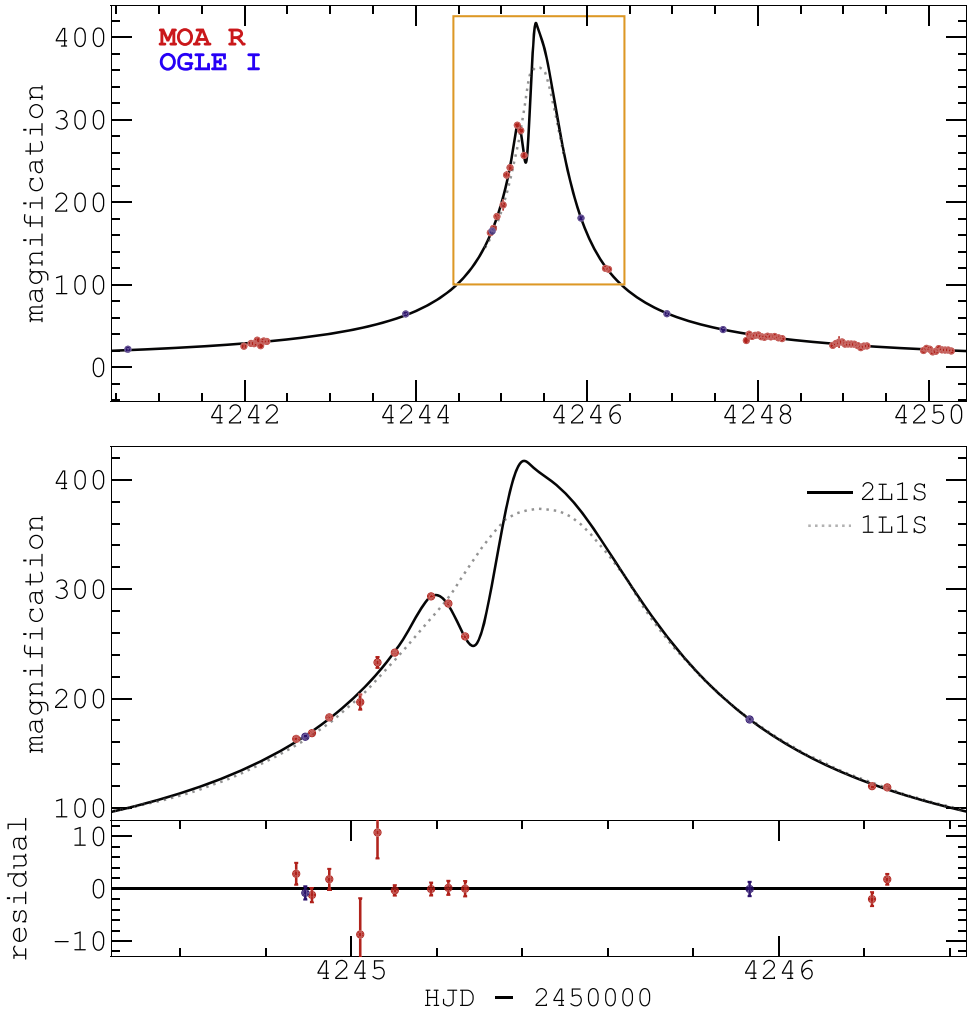

Figure 1. Best-fit light curve with constraints from the high-resolution follow-up data as described in Section 3. The 2L1S model shown is from the second column of Table 6 with $u_0 < 0$ and $s < 1$. The y-axis is given in flux units which are normalized to the $I_S = 21.8$ source star (e.g., "magnification") from the modeling.

Also, MOA have recently improved their photometry methods, so we have rereduced the MOA photometry following Bond et al. (2017). This rereduction includes corrections for systematic errors due to chromatic differential refraction (Bennett et al. 2012a). This has direct consequences on the microlensing model compared to the initial studies, which affects the fitting parameters like the microlensing parallax, the finite size of the source star, and other higher-order effects. Additionally, over the years we have refined our procedures to process, analyze, and calibrate AO data as well as update extinction-correction calculations. We will therefore adopt our standard method described by Beaulieu et al. (2018) and reanalyze the K_S NACO data.

Finally, we have obtained recent Keck-NIRC2 and HST observations in 2018 and 2023, which should give us the opportunity to independently resolve the source and lens and measure the magnitude and direction of their relative proper motion.

3. High-angular-resolution Follow-up with the Hubble Space Telescope and Keck

3.1. Preparing the Absolute Calibration Data Set

We use our own rereduction of data from the VVV survey (Minniti et al. 2010) obtained with the 4 m VISTA telescope at Paranal (Beaulieu et al. 2018). We cross-identified these JHK_S catalogs with the *VI* OGLE-III map (Udalski et al. 2015). We then obtained an OGLE-VVV catalog of 8500 objects with $VIJHK_S$ measurements, covering the footprint of the HST and Keck observations. We subsequently used this catalog to calibrate the HST and Keck data, and we also revisited the VLT/NACO data. Table 1 summarizes the HST and Keck observations that are presented for the first time in this work. These data span the years 2012–2023.

3.2. Keck-NIRC2

The target MB07192 was observed with the NIRC2 instrument on Keck II in the $K_{\rm short}$ band ($\lambda_c = 2.146\,\mu$m, hereafter *Ks*) on 2018 August 5 and 6. The two nights of data were combined using the KAI reduction pipeline (Lu 2022). The pipeline registers the images together, applies flat-field correction, dark subtraction, as well as bad pixel and cosmic-ray masking before producing the final combined image that we analyze. The data from both nights are of similar quality, with an average PSF FWHM of 66.2 mas for the August 5 data, and 67.5 mas for the August 6 data.

For the 2018 *Ks*-band observations, both the NIRC2 wide and narrow cameras were used. The pixel scales for the wide and narrow cameras are 39.69 mas pixel^{-1} and 9.94 mas pixel^{-1}, respectively. All of the images were taken using the Keck II laser

Table 1
New HST and Keck Observations in This Work

Epoch (UT) (yyyy-mm-dd)	Instrument	PA (deg)	Filter	T_{exp} (s)	N_{exp}	Δt (yr)	References
2012-03-30	WFC3−UVIS	131.8	F606W (V)	1760	8	4.85	(a)
			F814W (I)	1640	8	⋯	⋯
	WFC3−IR	131.8	F125W (J)	1412	8	⋯	⋯
	WFC3−IR	131.8	F160W (H)	1059	8	⋯	⋯
2014-03-30	WFC3−UVIS	131.8	F606W (V)	1760	8	6.85	(b)
			F814W (I)	1640	8	⋯	⋯
2018-08-06[a]	NIRC2	0.0	K_S	900	15	11.20	(c)
2023-08-06	WFC3−UVIS	309.5	F814W (I)	600	2	16.20	(d)

Notes. Δt gives the amount of time (in years) since the peak of the microlensing event.
[a] The 2018 epoch is from Keck; all other epochs are from HST.
References. (a) Bennett (2012b), (b) Bennett (2014), (c) Bennett (2018), (d) Sahu et al. (2023).

Table 2
HST, VLT NACO, and Keck Single-star PSF Photometry

Data Set	V	I	J	H	K_S
HST 2012	23.88 ± 0.02	20.93 ± 0.01	19.04 ± 0.01	18.28 ± 0.01	⋯
HST 2014	23.83 ± 0.02	20.90 ± 0.01	⋯	⋯	⋯
K12 NACO ep.1	⋯	⋯	19.21 ± 0.04	18.28 ± 0.04	17.95 ± 0.04
K12 NACO ep.2	⋯	⋯	19.32 ± 0.07	18.55 ± 0.11	17.99 ± 0.04
NACO ep.1	⋯	⋯	⋯	⋯	17.80 ± 0.05
NACO ep.2	⋯	⋯	⋯	⋯	17.92 ± 0.05
Keck 2018	⋯	⋯	⋯	⋯	17.88 ± 0.05
HST 2023	⋯	21.01 ± 0.04	⋯	⋯	⋯

Notes. We provide the magnitudes measured at the source position for MB07192. We recall the measured magnitudes from K12 for the two epochs. We underline that at the time of the first epoch, the source was still amplified by ∼0.15 mag. We reanalyzed the NACO K_S images and calibrated against VVV for the two epochs. Finally, we provide our flux calibration in K_S with Keck-NIRC2.

guide star AO system. For the narrow data, we combined 15 flat-field frames, six dark frames, and 15 sky frames for calibrating the science frames. A total of 15 *Ks*-band science frames with an integration time of 60 s per frame were reduced using KAI, which corrects instrumental aberrations and geometric distortion (Ghez et al. 2008; Lu et al. 2008; Yelda et al. 2010; Service et al. 2016).

Because of the potentially significant effects of a spatially varying PSF in ground-based AO imaging (Terry et al. 2023), we made a careful selection of bright and isolated reference stars that were then used to build the empirical PSF model. Each of the eight selected PSF reference stars has a magnitude $-0.7 < m < 0.7$ and separation $-4'' < r < 4''$ from the target. The resulting PSF model has a FWHM in the x- and y-directions of 6.8 pixels and 6.5 pixels, respectively.

Further, a coadd of four wide-camera images were used for photometric calibration using the catalog prepared in Section 3.1. The wide-camera images were flat-fielded, dark-current-corrected, and stacked using the `SWarp` software (Bertin 2010). We performed astrometry and photometry on the coadded wide-camera image using SExtractor (Bertin & Arnouts 1996), and subsequently calibrated the narrow-camera images to the wide-camera image by matching 80 bright isolated stars in the frames. The uncertainty resulting from this procedure is 0.05 mag. Table 2 gives the calibrated magnitudes for the target as measured in all high-resolution epochs detailed in this work.

3.3. The Extinction toward the Source star

The OGLE extinction calculator is a standard way to estimate the extinction for a galactic bulge field, and it has been commonly used for many years.[15] The calculator is derived from the reddening and extinction study of Nataf et al. (2013). For MB07192, the calculator gives $E(V-I) = 1.10 \pm 0.127$ and an extinction $A_I = 1.3$. These standard extinction maps have recently been superseded by Surot et al.'s (2020) analysis of the VVV survey, and give $E(J-Ks) = 0.329 \pm 0.018$ at the location of the target. We then follow Nataf et al. (2013) in adopting $E(J-K_S)/E(V-I) = 0.3433$ and $A_I = 0.7465E(V-I) + 1.37E(J_{K_S})$, with which we derive the extinctions. Following Nishiyama et al. (2009), we obtain the extinctions summarized in Table 3 along with prior estimates from the literature. For our subsequent analysis, we adopt the numbers from the last row of Table 3 (i.e., this work).

3.4. Resolving the Source and Lens in Keck/NIRC2

Given the lens detections from HST 2012 and 2014 data, the lens and source stars have a predicted separation of $0.65 \times$ FWHM in 2018. We expect the stars to be partially resolved, so it is necessary to use a PSF fitting routine to measure both targets separately. Following the methods of Bhattacharya et al. (2018) and Terry et al. (2021), we use a modified version of the `DAOPHOT-II` package (Stetson 1987), which we call `DAOPHOT_MCMC`, to run Markov Chain Monte Carlo (MCMC) sampling on the pixel grid encompassing the blended targets. Further details of the MCMC routine are given in Terry et al. (2021, 2022).

[15] https://ogle.astrouw.edu.pl/cgi-ogle/getext.py

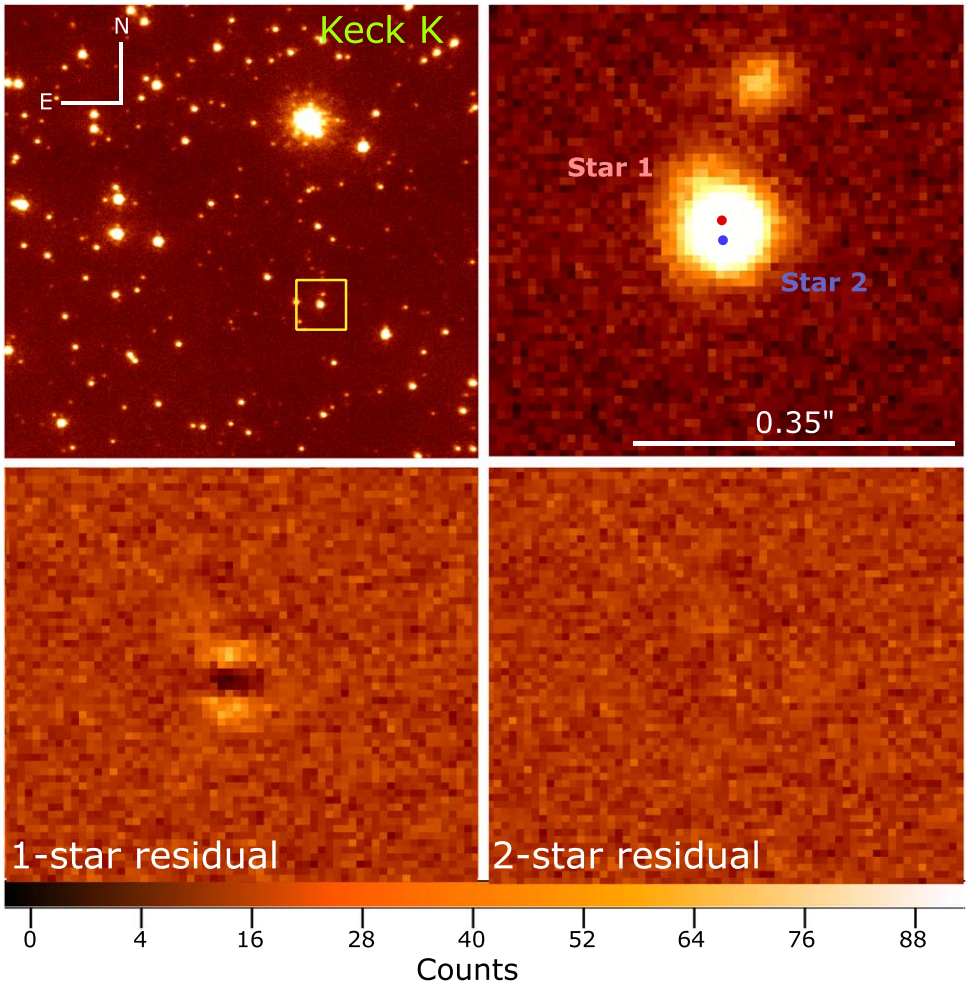

Figure 2. Top left: the coadded sum of 15 Keck-NIRC2 narrow-camera images, each with an exposure time of 60 s. The target is indicated with a square outline. Top right: zoomed image of the MB07192 blended source and lens stars. The magnitude of the separation in this epoch is 29.3 ± 1.1 mas. Bottom left: the residual image from a single-star PSF fit with DAOPHOT. A clear signal is seen due to the blended stellar profiles. Bottom right: the residual image for a simultaneous two-star PSF fit, showing a significantly improved subtraction. The color bar represents the pixel intensity (or counts) in the bottom panel residual images.

Table 3
Extinction Estimates toward the Source

Ext. Map	$E(V-I)$	$E(J-K_s)$	A_V	A_I	A_J	A_H	A_{KS}
B08	1.12 ± 0.09	···	2.73 ± 0.13	1.61 ± 0.10	···	···	···
K12		0.43 ± 0.14	···	···	0.72 ± 0.10	0.46 ± 0.10	0.29 ± 0.10
Ext. calc	1.10 ± 0.13	·····	2.43 ± 0.16	1.33 ± 0.1	···	···	···
This study	**1.10 ± 0.06**	**0.33 ± 0.02**	**2.45 ± 0.15**	**1.35 ± 0.07**	**0.44 ± 0.02**	**0.24 ± 0.01**	**0.11 ± 0.01**

Notes. We summarize here the different estimates for the extinction toward the source, in the initial study (B08), the follow-up work with NACO data (K12), and this study (bold values). Extinction values are derived from a combination of the methods described in Nishiyama et al. (2009), Bennett et al. (2010), Nataf et al. (2013), and Surot et al. (2020); see Section 3.3.

The stellar profile does not appear to be significantly extended in the NIRC2 data, as seen in the top-right panel of Figure 2. However, using `DAOPHOT_MCMC` to fit a single-star PSF to the target produces the residual seen in the lower-left panel of Figure 2, which shows a strong signal due to extended flux from the blended star (presumed lens). Rerunning the routine in the two-star fitting mode (e.g., simultaneously fitting two PSF models) produces a significantly better fit, as expected, with a χ^2 improvement of $\Delta\chi^2 \sim 784$. The two-star residual is nearly featureless, as can be seen in the lower-right panel of Figure 2. Table 4 shows the calibrated magnitudes for the two stars of $K_1 = 18.94 \pm 0.10$ and $K_2 = 18.39 \pm 0.09$.

The final error bars on the Keck photometry and astrometry, which we report in Tables 4 and 5, are determined with a combination of MCMC and jackknife errors. The jackknife method (Quenouille 1949, 1956; Tierney & Mira 1999) allows us to determine uncertainties due to PSF variations between individual Keck images. From the total of 15 Keck images, we construct $N = 14$ coadded jackknife images, with each combined image containing all but one successive image in

Table 4
HST and Keck Multi-star PSF Photometry

Star	V Mag.	I Mag.	K Mag.
Star 1 (Lens)	24.93 ± 0.32	21.56 ± 0.15	18.39 ± 0.09
Star 2 (Source)	24.25 ± 0.18	21.68 ± 0.16	18.94 ± 0.10
Lens + Source	23.79 ± 0.04	20.87 ± 0.02	17.88 ± 0.05

Note. V and I magnitudes are calibrated to the OGLE-III system and K magnitudes are calibrated to the 2MASS system, as described in Section 3.

Table 5
Measured Lens–Source Separations from HST and Keck

	Separation (mas)		
Year	East	North	Total
2012 (HST V)	2.28 ± 4.60	15.58 ± 4.96	15.75 ± 6.78
(HST I)	1.01 ± 1.39	18.17 ± 1.71	18.20 ± 2.23
2014 (HST V)	9.84 ± 4.74	22.17 ± 4.01	24.26 ± 6.22
(HST I)	3.12 ± 1.23	21.62 ± 1.03	21.84 ± 1.63
2018 (Keck K)	-0.34 ± 1.03	29.37 ± 1.01	29.38 ± 1.46
2023 (HST I)	-1.97 ± 1.49	43.13 ± 1.68	43.17 ± 2.26
	$\mu_{\mathrm{rel,H,E}}$ (mas yr^{-1})	$\mu_{\mathrm{rel,H,N}}$ (mas yr^{-1})	$\mu_{\mathrm{rel,H}}$ (mas yr^{-1})
Weighted mean	0.63 ± 0.29	2.76 ± 0.27	2.83 ± 0.37

each iteration. This method is also sometimes called the "drop-one" or "leave-one-out" method. The jackknife errors are then calculated via the equation

$$\sigma_x = \sqrt{\frac{N-1}{N}\sum(x_i - \bar{x})^2}\,, \quad (1)$$

where x_i is a given value for the ith jackknife image, and $\bar{x}$ is the mean value for the jackknife images; see Bhattacharya et al. (2021) and Terry et al. (2022) for further details on the jackknife method.

From the dual-star PSF fitting in Keck, we find a difference in K-band magnitude between the two blended stars of $K_{S1} - K_{S2} = -0.55 \pm 0.13$. Since the two stars are similar enough magnitude in K, at this point we simply apply arbitrary labels of "Star 1" and "Star 2" to the two stars in Keck. However, our subsequent analysis of the HST data will allow us to confidently determine which star is the source and which is the lens (Section 3.8).

3.5. HST WFC3/UVIS: 2012, 2014, and 2023 Data

The target MB07192 was observed a total of three times with the Wide Field Camera 3 (WFC3)/UVIS camera on the HST. The first observation took place on 2012 February 23 in the F555W, F814W, F125W, and F160W filters. A second epoch of observations took place on 2014 March 30 with the same four filters, and finally a third epoch was obtained on 2023 August 6 with just two exposures in the F814W filter. The data sets are from proposals GO-12541 (PI: Bennett), GO-13417 (PI: Bennett), and GO-16716 (PI: Sahu), and were obtained from the Mikulski Archive for Space Telescopes (MAST). We flat-fielded, stacked, corrected for distortions, and performed PSF photometry with the program DOLPHOT (Dolphin 2016). Because of the disparate sensitivities, the visible images obtained with the UVIS module (F555W and F814W) and the near-IR images obtained with the IR module (F125W and F160W; Section 3.6) were reduced separately.

The drizzled, stacked frames with the astrometric solutions from the Space Telescope Science Institute (STScI) were used as the reference image for source finding. We used DOLPHOT to correct for pixel area distortions, remove cosmic rays, and perform PSF fitting photometry of the individual frames. Because of the crowded nature of the field, the sky background was determined iteratively, and many artifacts due to bright stars were rejected. DOLPHOT uses a library of reference PSFs for each filter and applies a perturbation to the $N \times N$ array of PSFs based on differences between the PSF present in the image and the library PSF (Anderson & King 2006). This perturbation typically adjusts the central pixels of the PSF by a few percent, where this difference comes mostly from telescope breathing or jitter. The PSF-fit magnitudes are corrected to a standard circular aperture of radius $0\farcs5$ and matched across all filters. In order to eliminate marginal detections and stars badly impacted by bright neighbors, we rejected stars with signal-to-noise ratio < 5 and crowding parameter >0.75 as well as any objects flagged by the software as too sharp or too extended to be stellar. The output magnitudes are given in the STScI VegaMag system (m555, m814, m125, and m160). Note that we used only main-sequence stars for calibration, and ignore color terms between VVV and the STScI VegaMag system.

3.6. HST WFC3/IR: 2012 Data

For the 2012 HST epoch, the WFC3-IR channel was utilized to take eight exposures with the F125W ($\lambda_c = 1.248\ \mu$m) filter and eight exposures with the F160W ($\lambda_c = 1.537\ \mu$m) filter. These are wide J- and H-band filters, respectively. Similar to the reduction procedure described in Section 3.5, DOLPHOT was used for flat-fielding, distortion corrections, pixel area map corrections, cosmic-ray rejection, and PSF fitting, which gives the resulting photometry and astrometry for all detected sources in the field.

In contrast to the WFC3-UVIS and Keck/NIRC2 data, the source and lens were not independently resolved in the WFC3-IR data. This is primarily due to the much larger pixel size in near-IR HST images ($\sim$100 mas pix^{-1}), and the fact that the only WFC3-IR data were taken in the earliest HST epoch (2012) when the lens and source were more highly blended than they were in the 2014 or 2023 HST epochs. It is likely the lens and source may have been at least partially resolved if near-IR data were taken in 2014, and very likely in 2023. Details of the 2012 WFC3-IR visit can be found in Table 1, and the single-star PSF photometry for the target (source and lens) can be found in columns (4) and (5) of Table 2.

Lastly, given the calibrated J- and H-band magnitudes we measured for the combined source and lens in the WFC3-IR images, we measured the excess flux at the position of the source in these passbands to estimate the lens (e.g., blend) star magnitude. This assumes all of the blended light comes from the lens, but we can be confident that this is the case since we have multiepoch direct lens detections in the other HST and Keck data sets. Appendix D includes Figure 12, which shows the color–magnitude diagram (CMD) for all of the detected sources in the HST field, as well as the estimated J- and H-band magnitudes and colors for the source and lens.

3.7. HST Multiple-star PSF Fitting

In addition to the photometry obtained using DOLPHOT, we performed multi-star PSF fitting on the target in all three of the HST epochs. Since the 2012 and 2014 epochs are approximately 6.4 and 4.4 yr before the Keck observations, we expect the separation between the source and lens star to be 0.619× and 0.734× smaller in these HST images compared to Keck. This is due primarily to the relative proper motion between the source and lens star as observed from Earth (and HST). Similarly, the 2023 HST images were taken approximately 5 yr after the Keck observations, so we expect the lens and source separation to be 1.445× larger in this epoch than the Keck images. Because each HST observation is separated by at least several years and some epochs were taken at different position angles (PAs), we performed coordinate transformations between the Keck observation and each of the HST observations independently. We do this by cross-matching approximately two dozen isolated and bright (but not saturated) stars in each data set, and then calculating the linear (i.e., first-order) transformation between the pixel positions in the HST and Keck catalogs. The transformations are listed as follows:

$$\begin{aligned}
2012:\quad & x_{\rm hst} = -0.170x_{\rm keck} + 0.186y_{\rm keck} + 804.011\\
& y_{\rm hst} = -0.184x_{\rm keck} - 0.169y_{\rm keck} + 1175.664\\
2014:\quad & x_{\rm hst} = -0.169x_{\rm keck} + 0.186y_{\rm keck} + 802.920\\
& y_{\rm hst} = -0.185x_{\rm keck} - 0.169y_{\rm keck} + 1175.561\\
2023:\quad & x_{\rm hst} = 0.164x_{\rm keck} - 0.188y_{\rm keck} + 283.268\\
& y_{\rm hst} = 0.187x_{\rm keck} + 0.166y_{\rm keck} + 225.342.
\end{aligned}$$

The average rms scatter for these relations is $\sigma_x \sim 0.25$ and $\sigma_y \sim 0.20$ HST/UVIS pixels for the same 16 stars used in each transformation. Given the varying baseline between the earliest and latest HST epochs and the 2018 Keck epoch, this scatter of ∼13 mas can be mostly explained by an average proper motion of ∼2.5 mas yr^{-1} in each direction. We note the 2012 and 2014 data were taken with the larger subarray chip, UVIS2-2K2C-SUB, while the recent 2023 data were taken with the smaller chip, UVIS2-C1K1C-SUB. Using the smaller subarray chip allows us to minimize the negative effect of charge transfer efficiency, since the detector has degraded between the 2012/2014 and 2023 epochs.

This HST analysis was performed using a modified version of the codes developed in Bennett et al. (2015) and Bhattacharya et al. (2018), which analyzes the original individual images with no resampling. This avoids any loss in resolution that can occur when dithered, undersampled images are combined. The top-left panel of Figure 3 shows the target and surrounding HST stars from the combined *I*-band image in 2014. A zoom on the target is shown in the top-right panel, which also shows an unrelated star to the north of MB07192. The lower panels of Figure 3 show the residual images after fitting a single PSF model and simultaneously fitting two PSF models to the blended stars. The single-star residual shows the typical signal that we would expect for two highly blended stars. The direction and amplitude of the measured separation here is consistent with the 2018 detection in Keck (Table 5). The *V*-band detection is at a lower confidence than the *I*-band detection (∼2σ versus >5σ above the noise level). This leads to a larger error on the measured *V*-band lens magnitude (Table 4) and significantly larger error on the measured lens–source separations in the HST *V* band (see Table 5).

Given the strong detection in the Keck data, we impose separation constraints when analyzing the earlier HST epochs, particularly the 2012 epoch in the *V* band, where the lens detection is most marginal. We convert the Keck relative proper-motion value ($\mu_{\rm rel,H} = 2.63 \pm 0.13$ mas yr^{-1}) to constraints on the position of the lens and source in the 2012 HST images, while taking into account the 4.8520 yr between the microlensing event peak and the 2012 Hubble observations. We note that in all of our HST PSF fitting procedures we include the unrelated faint nearby neighbor as a third star to avoid any interference of its PSF with our measurement of lens–source separation. Between the 2012 and 2023 epochs, the unrelated neighbor star moves ∼1 HST pixel closer to MB07192.

For all three HST epochs (2012, 2014, and 2023), the F814W fits converge to a consistent solution with "Star 1" to the north as the slightly brighter star ($\Delta m_{\rm F814W} \sim 0.1$). For the two epochs of F555W data (2012 and 2014), the PSF fit converged to a unique solution in the 2014 data without requiring any separation constraint, though the 2012 fit required a separation constraint to be imposed, as mentioned previously. In all HST F814W fits, "Star 2" to the south is slightly fainter than "Star 1." Our reduction and fitting code places the star coordinates from both filters into the same reference system, so all stars have positions that are consistent between both passbands. The best-fit magnitudes (calibrated to OGLE *V* and *I*) from the 2014 HST epoch are given in Table 4, and the best-fit positions in all epochs and filters are given in Table 5.

The HST data were calibrated to the OGLE-III catalog (Szymański et al. 2011) using eight relatively bright isolated OGLE-III stars that were matched to HST stars. The same eight stars were used in each epoch. For the best-quality HST data in both filters (i.e., the 2014 epoch), the calibrations yielded $I_1 = 21.56 \pm 0.15$, $V_1 = 24.93 \pm 0.32$, $I_2 = 21.68 \pm 0.16$, and $V_2 = 24.25 \pm 0.18$. The magnitude of both lens and source stars combined is measured to significantly higher precision, $I_{12} = 20.87 \pm 0.02$ and $V_{12} = 23.79 \pm 0.04$. This combined magnitude allows us to place a stronger constraint when reevaluating the light-curve photometry. During our PSF fitting, the two blended stars can trade flux back and forth, which results in larger errors on the individual stars' magnitude.

3.8. Identifying the Source and Lens Stars

With the HST *V*- and *I*-band measurements described in Section 3.7, we can now attempt to determine which star is the source and which is the lens. As mentioned previously, since the original discovery paper of Bennett (2008), the MOA group has begun detrending its photometry to remove systematic errors caused by differential atmospheric refraction (Bennett & Rhie 2002; Bond et al. 2017). Following Bond et al. (2017), we correct the MOA photometric data and perform remodeling of the MOA + OGLE photometry. This reanalysis yields an estimate of the source star *I*-band magnitude of $I_S = 21.8 \pm 0.05$ with a color of $V_S - I_S = 2.7 \pm 0.2$. This source *I*-band magnitude is within 1σ of the HST *I*-band magnitude for "Star 2," and just over 1σ fainter than the HST *I*-band magnitude for "Star 1." Additionally, this estimated source color is a closer match to the measured HST $V - I$ color of

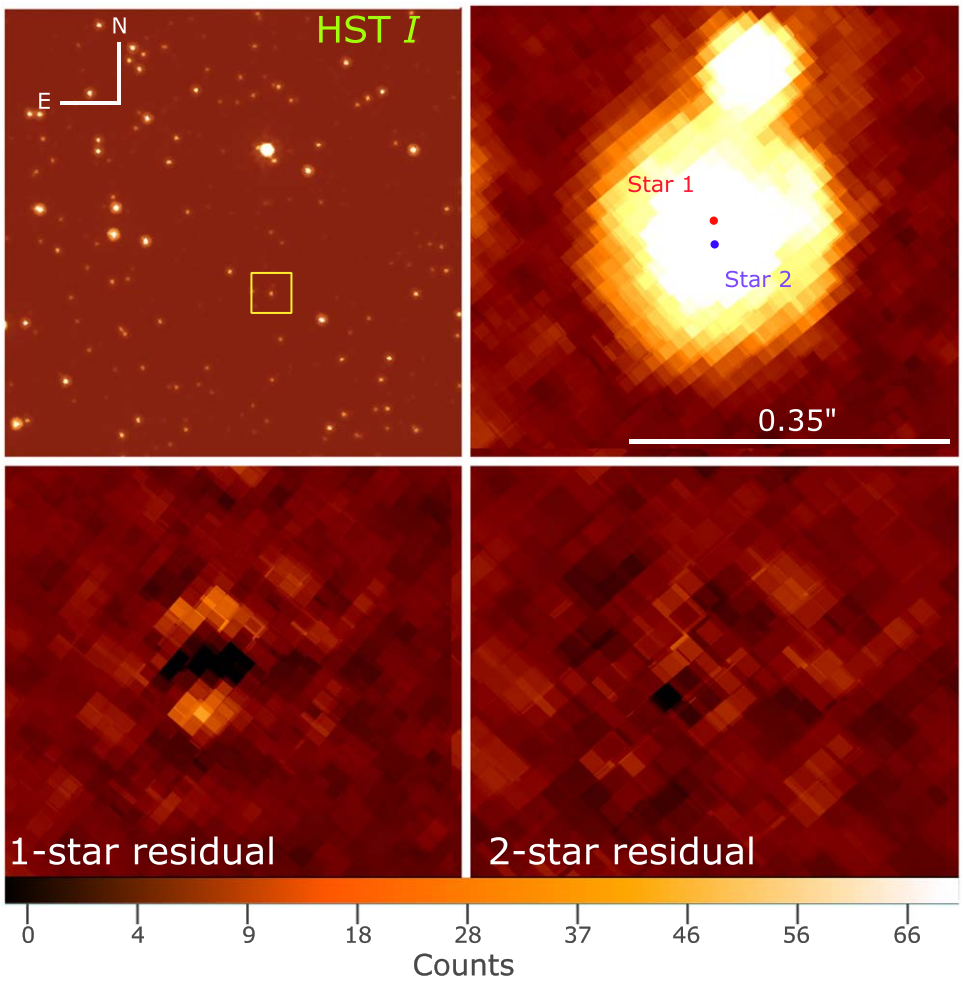

Figure 3. Similar to Figure 2, but for the 2014 HST data (eight exposures). The zoomed inset and residual image panels show 100 × 100 supersampled pixels where the observed dither offsets are accurate to 0.01 pixels. The color bar represents the pixel intensity (counts) seen in the top-right and lower-left/lower-right panels.

"Star 2" (2.57 ± 0.24), as can be seen in Figure 4. These results support the identification of "Star 2" as the true source star. However, since the ground-based V-band estimate of the source comes from a relatively weak relationship (OGLE-I–MOA-R), we conduct a further verification of the source and lens using their relative proper motions as measured in HST and Keck.

We calculate the 2D prior probability distribution of the lens–source relative proper motion ($\mu_{\rm rel}$) using the Koshimoto et al. (2021) Galactic model to determine which stars are the preferred lens and source. Figure 5 shows this proper-motion distribution for MB07192, with two locations for the possible lens (the "North" or "South" star). We calculate these $\mu_{\rm rel}$ priors from the distribution of single-lens stars that reproduces the Einstein radius crossing time that accounts for the host-star mass in a binary-lens case, i.e., $t_E/\sqrt{1+q}$. The results show that there is a preference for the "North star" to be the true lens star considering the stellar distribution along this sight line. The relative probability is $P_N/P_S = 25.88/12.43 = 2.08$; this means the "North star" is $>2\times$ more likely to be the lens than the "South star." So, given the locations of "Star 2" and "Star 1" on the CMD (before relabeling them) and the relative proper-motion prior probability distribution (Figure 5), we identify "Star 2" (e.g., the "South star") to be the true source star and "Star 1" (e.g., the "North star") to be the true lens star which hosts the planet. We subsequently label the source and lens on the CMD in Figure 4 as well as the stars in Table 4.

4. Lens–Source Relative Proper Motion

The Keck (2018) and HST (2012, 2014, 2023) follow-up observations were taken between 4.85 and 16.20 yr after the peak magnification, which occurred in 2007 May. The motion of the source and lens on the sky is the primary cause for their apparent separation; however, there is also a small component that can be attributed to the orbital motion of Earth (e.g., trigonometric parallax). As this effect is of order $\leqslant$0.10 mas for a lens at a distance of $D_L \geqslant 2$ kpc, we are safe to ignore this contribution in our analysis as it is much smaller than the error bars on the stellar position measurements (e.g., the astrometric measurements given in Table 5). The mean lens–source relative proper motion is measured to be $\mu_{\rm rel,H} = (\mu_{\rm rel,H,E},\ \mu_{\rm rel,H,N}) = (0.634 \pm 0.291,\ 2.761 \pm 0.274)$ mas yr^{-1}, where the "H" subscript indicates that these measurements were made in the heliocentric reference frame, and the "E" and "N" subscripts represent the east and north on-sky directions, respectively.

Our light-curve modeling is performed in the geocentric reference frame that moves with the Earth at the time of the event peak. Thus, we must convert between the geocentric and heliocentric frames by using the relation given by Dong et al. (2009):

$$\mu_{\rm rel,H} = \mu_{\rm rel,G} + \frac{\nu_\oplus \pi_{\rm rel}}{AU}, \quad (2)$$

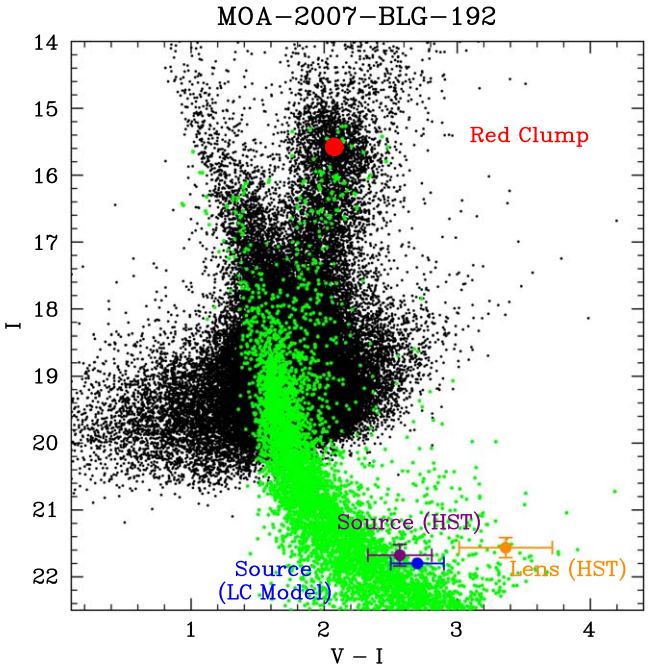

Figure 4. The observed color–magnitude diagram (CMD) for the MB07192 field. The OGLE-III stars within 90″ of MB07192 are shown in black, with the HST CMD of all detected sources from the 2014 epoch shown in green. The red point indicates the location of the red clump centroid, and the purple and orange points show the source and lens colors and magnitudes from the 2014 HST observations. The blue point indicates the source star magnitude and color given by the original light-curve modeling.

where $\nu_{\oplus}$ is Earth's projected velocity relative to the Sun at the time of peak magnification. For MB07192, this value is $\nu_{\oplus \mathrm{E,N}} = (25.772,\ \ 1.237)\,\mathrm{km\,s^{-1}} = (5.433,\ \ 0.261)\,\mathrm{au\,yr^{-1}}$ at $\mathrm{HJD}' = 4245.45$, where HJD '= HJD−2,450,000. With this information and the relative parallax relation $\pi_{\mathrm{rel}} \equiv AU(1/D_L - 1/D_S)$, we can express Equation (2) in a more convenient form:

$$\mu_{\mathrm{rel,G}} = \mu_{\mathrm{rel,H}} - (5.433,\ \ 0.261) \times (1/D_L - 1/D_S)\ \mathrm{mas\ yr^{-1}}, \tag{3}$$

where D_L and D_S are the lens and source distance, respectively, given in kiloparsecs. We have directly measured $\mu_{\mathrm{rel,H}}$ from the HST and Keck data, so this gives us the relative proper motion in the geocentric frame of $\mu_{\mathrm{rel,G}} = 3.10 \pm 0.19\ \mathrm{mas\ yr^{-1}}$. As a reminder, the lens and source distance we use in Equation (2) are inferred by the best-fit light-curve results, which include constraints from the high-resolution imaging.

5. Lens System Properties

As has been shown in prior work (Bhattacharya et al. 2018; Bennett et al. 2020; Terry et al. 2021; Rektsini et al. 2024), we find it particularly useful to apply constraints from the high-resolution follow-up observations to the light-curve models (we deem this "image-constrained modeling"). This can help prevent the light-curve modeling from exploring areas in the parameter space that are excluded by the high-resolution follow-up observations. We refer the reader to Bennett et al. (2023) for a full description of the methodology for applying these constraints to the modeling and an exhaustive list of the light-curve and high-resolution imaging parameters that are important for obtaining full solutions for planetary lens systems in this context.

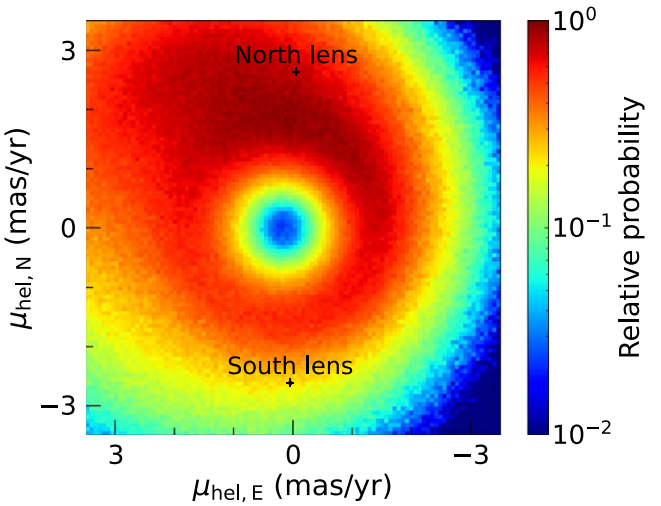

Figure 5. The probability distribution for the north and east components of lens–source relative proper motion (μ_{rel}) using the Galactic model from Koshimoto et al. (2021) and `genulens` (Koshimoto & Ranc 2021). The possible lens positions (north and south) are plotted in black and given by the relative motion of the two stars detected in the HST and Keck data. Importantly, this distribution uses t_{E} values that are close to the measured t_{E} value from the light-curve modeling ($t_{\mathrm{E}} \sim 99.5$ days). This implies that the "North star" is >2× more likely to be the lens than the "South star."

We use the python package `eesunhong` for the light-curve modeling to incorporate constraints on the brightness and separation of the lens and source stars from the high-resolution imaging via HST and Keck (Bennett & Rhie 1996; Bennett 2010; Bennett et al. 2023). Ideally, we want to use a mass–distance relation coupled with empirical mass–luminosity relations to infer the mass and distance of the host star. In order to do this, we need to know the distance to the source star, D_S. Thus, we are required to include the source distance as a fitting parameter in the remodeling of the light curve with imaging constraints. We include a weighting from the Koshimoto et al. (2021) Galactic model as a prior for D_S, and we also use the same Galactic model to obtain a prior on the lens distance for a given value of D_S. This prior is not used directly in the light-curve modeling, but instead is used to weight the entries in a sum of Markov Chain values.

The angular Einstein radius, θ_{E}, and the microlensing parallax vector, $\boldsymbol{\pi}_{\mathrm{E}}$, give relations that connect the lens system mass to the source and lens distances, D_S and D_L (B08; Gaudi 2012). The relations are given by

$$M_L = \frac{c^2}{4G}\theta_{\mathrm{E}}^2 \frac{D_S D_L}{D_S - D_L}, \tag{4}$$

and

$$M_L = \frac{c^2}{4G}\frac{\mathrm{AU}}{\pi_E^2}\frac{D_S - D_L}{D_S D_L}, \tag{5}$$

where M_L is the lens mass, and G and c are the gravitational constant and speed of light, respectively. As mentioned previously, the measurement of $\mu_{\mathrm{rel,H}}$ from the high-resolution imaging allows us to measure $\mu_{\mathrm{rel,G}}$ to high precision, which ultimately lets us determine $\boldsymbol{\theta}_{\mathrm{E}} \sim \boldsymbol{\mu}_{\mathrm{rel,G}} \times \boldsymbol{t}_{\mathrm{E}}$. Additionally, the two components of the μ_{rel} measurement enables a much tighter constraint on the possible values of $\pi_{\mathrm{E,N}}$. The north

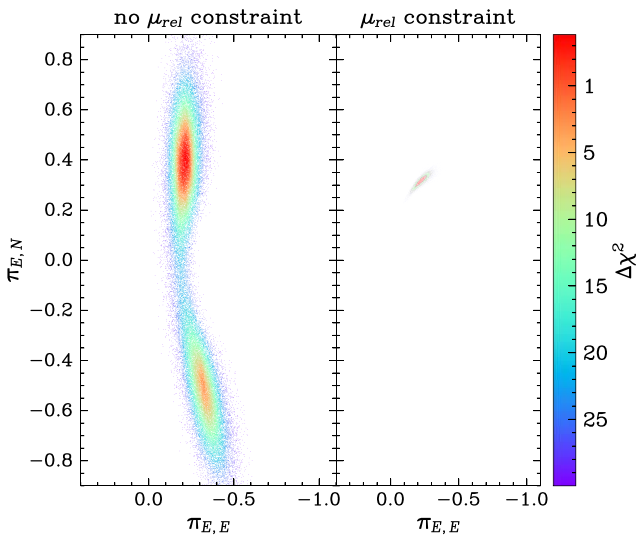

Figure 6. Left: the MCMC distribution for $\pi_{\rm E}$ from the light-curve modeling without any constraint from the high-resolution imaging. Right: the MCMC distribution for $\pi_{\rm E}$ from the light-curve modeling with the inclusion of high-resolution imaging constraints. The color bar represents the χ^2 differences from the best-fit light-curve model. The two components of the relative proper motion that were measured by HST and Keck allow the north component, $\pi_{\rm E,N}$, to be tightly constrained.

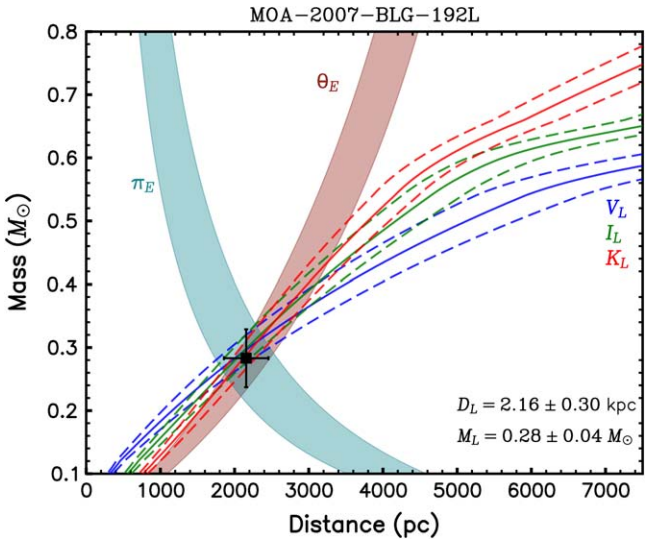

Figure 7. The mass–distance relation for MB07192L with constraints from the lens flux measurement in HST V (blue), HST I (green), and Keck K (red). Dashed lines show the 1σ error bars for each passband. The solid teal region shows the mass–distance relation calculated using the microlensing parallax measurement ($\pi_{\rm E}$), and the solid brown region shows the mass–distance relation calculated using the angular Einstein radius measurement ($\theta_{\rm E}$).

direction in particular is usually only weakly constrained because it is typically perpendicular to the orbital acceleration of the observer for microlensing events toward the Galactic bulge. The geocentric relative proper motion and the microlensing parallax are related by

$$\pi_E = \frac{\pi_{\rm rel}}{t_E}\frac{\mu_{{\rm rel},G}}{|\mu_{{\rm rel},G}|^2}, \quad (6)$$

so with the measurement of $\pi_{\rm E,E}$ and $\mu_{\rm rel,H}$, we can use Equations (2) and (6) to solve for $\pi_{\rm E,N}$. This tight constraint on the north component of the microlensing parallax can be seen in Figure 6, where the left panel shows the distribution in $\pi_{\rm E,N}$ is largely unconstrained. When the constraint from the high-resolution measurement of $\mu_{\rm rel}$ is applied, the distribution collapses to a relatively small region centered on $\pi_{\rm E,N} \sim 0.3$.

Additionally, since we have a direct measurement of lens flux in the V, I, and K bands, we utilize the Delfosse et al. (2000) empirical mass–luminosity relations in each of these passbands as described by Bennett et al. (2018). We consider the foreground extinction in each passband (i.e., Table 3) and generate the relations in conjunction with the mass–distance relations given by Equations (4) and (5). Figure 7 shows the measured mass and distance of the MB07192 lens. The blue (HST V), green (HST I), and red (Keck K) curves represent the mass–distance relations obtained from the empirical mass–luminosity relations with lens flux measurements given in Table 4. The dashed lines represent the 1σ error from the Keck and HST measurements. Further, the mass–distance relation obtained from the measurement of $\theta_{\rm E}$ (i.e., Equation (4)) is shown as a solid brown region. Considering only these two relations (empirical mass–luminosity and $\theta_{\rm E}$), there is overlap for a significant amount of mass and distance space. This is sometimes referred to as the "continuous degeneracy" (Gould 2022). Fortunately, this degeneracy is broken when we include the constraint from the microlensing parallax measurement, $\pi_{\rm E}$, shown as the solid teal region in Figure 7.

Table 6 shows the results of the four degenerate light-curve models and the Markov Chain average for all four models. Although we are able to successfully reduce the number of possible binary-lens solutions presented in K12 by a factor of 2, the close/wide and u_0 degeneracies still remain. Further, the host-star mass is very precisely measured now, however the best-fit mass ratio, q, remains largely uncertain because of poor sampling of the light curve. Table 7 gives the derived lens system physical parameters along with their 2σ ranges. The large error on the mass ratio results in a large error in the inferred planet mass (see Table 7). The lens system properties (host mass, planet mass, etc.) shown in Table 7 and Figure 8 are derived from the combined cumulative probability distributions that incorporate the MCMC distributions given by all of the models (e.g., Table 6 columns), weighted by their respective χ^2 fit values.

Further, the caustic-crossing models are disfavored by a total of $\Delta\chi^2 \sim 13$. Since this difference is not particularly large, we include the possible caustic-crossing models in our MCMC sums. However, they do not significantly change the overall results, and they have a very low weighting of $e^{\frac{-\chi^2}{2}} = 0.0015$. The χ^2 differences are spread across many parameters; some of the largest contributors come from source magnitudes ($\Delta\chi^2 = 1.19$), source distance ($\Delta\chi^2 = 3.24$), and the photometric light-curve fit itself ($\Delta\chi^2 = 7.95$). Lastly, we note that the caustic-crossing models span a relatively small volume in parameter space, which can be clearly seen from Figure 5 of B08. All of these factors contribute to the overall low likelihood for any of the caustic-crossing models in this event.

The MB07192 lens system is located at a distance of $\sim$2.2 kpc and has a log mass ratio of $\log_{10}(q) = -3.87 \pm 0.53$. The host star is directly detected in several high-resolution imaging passbands, enabling us to precisely measure its mass to be $M_{\rm host} = 0.28 \pm 0.04\ M_\odot$, with a less precisely measured mass of the planet to be $m_{\rm planet} = 12.49^{+65.47}_{-8.03}\ M_\oplus$. These masses are consistent with a planet with mass between a super-Earth and sub-Saturn orbiting an M4V dwarf star near the

Table 6
Best-fit Model Parameters with $\mu_{\rm rel}$ and Magnitude Constraints

Parameter	$u_0 < 0$		$u_0 > 0$		MCMC Averages
	$s < 1$	$s > 1$	$s < 1$	$s > 1$	
$t_{\rm E}$ (days)	99.469	98.722	100.111	99.262	99.577 ± 3.919
t_0 (HJD')	4245.446	4245.448	4245.431	4245.436	4245.440 ± 0.0070
u_0	−0.0027	−0.0029	0.0035	0.0004	-0.0027 ± 0.0012
			($u_0 > 0$)		0.00195 ± 0.00155
s	0.9102	1.0311	0.8780	1.1441	0.8728 ± 0.0667
			($s > 1$)		1.0951 ± 0.0938
α (rad)	2.1061	1.9288	4.5473	3.2862	2.4364 ± 0.5075
			($u_0 > 0$)		3.9167 ± 0.6305
log(q)	−3.9751	−3.9975	−3.6017	−3.7937	-3.8690 ± 0.5253
t_* (days)	0.0562	0.0539	0.0567	0.0547	0.0551 ± 0.0044
$\pi_{\rm E,N}$	0.3161	0.3152	0.3119	0.3133	0.3154 ± 0.0218
$\pi_{\rm E,E}$	−0.2364	−0.2308	−0.2338	−0.2300	-0.2359 ± 0.0474
$D_{\rm s}$ (kpc)	7.8423	7.1562	6.9687	7.1156	7.049 ± 1.163
Fit χ^2	4760.94	4760.97	4761.45	4761.53	

Table 7
Lens System Properties with Lens Flux Constraints

Parameter	Units	Values and rms	2σ Range
Angular Einstein radius ($\theta_{\rm E}$)	mas	0.854 ± 0.043	0.775–0.947
Geocentric lens–source relative proper motion ($\mu_{\rm rel,G}$)	mas yr^{-1}	3.14 ± 0.15	2.84–3.44
Host mass ($M_{\rm host}$)	$M_\odot$	0.28 ± 0.04	0.23–0.37
Planet mass ($m_{\rm p}$)	$M_\oplus$	$12.49^{+65.47}_{-8.03}$	2.75–105.06
2D separation ($a_\perp$)	au	2.02 ± 0.44	1.26–2.86
3D separation ($a_{\rm 3d}$)	au	$2.44^{+1.39}_{-0.68}$	1.38–9.65
Lens distance (D_L)	kpc	2.16 ± 0.30	1.75–2.76
Source distance (D_S)	kpc	7.05 ± 1.17	4.83–9.38

bottom of the main sequence for the redder, foreground disk star population (Figure 4). Figure 8 shows the final posterior probability distributions for the planetary companion mass, host-star mass, 2D projected separation, and lens system distance. We note the most likely mass for the planet is in the super-Earth regime (∼3–12 $M_\oplus$), as given by the top-left panel in Figure 8. The best-fit solution gives a 2D projected separation of $a_\perp = 2.02 \pm 0.44$ au. These physical parameters are calculated from the best-fit solution, which takes a combined weighting of several models along with a Galactic model prior based on Koshimoto et al. (2021).

6. Discussion and Conclusion

Our high-resolution follow-up observations of the microlensing target MB07192 have allowed us to make a direct measurement of the lens system flux in multiple passbands (V, I, and K) as well as a precise determination of the amplitude and direction of the lens–source relative proper motion $\mu_{\rm rel}$. We perform simultaneous multiple-star PSF fitting to obtain best-fit positions and fluxes for both stars across two independent platforms (HST and Keck). The lens flux measurements we make enable us to use mass–luminosity relations and new constraints on higher-order light-curve effects ($\pi_{\rm E}$ and $\theta_{\rm E}$) to measure a precise mass and distance for the lens system.

Further, we demonstrate the importance of applying constraints from high-resolution follow-up imaging on the microlensing light-curve modeling. In particular, the microlensing parallax effect, which is present in all microlensing events observed from a heliocentric reference frame, is tightly constrained when the direction of $\mu_{\rm rel}$ can be measured through high-resolution imaging. This measurement is critically important for several reasons. First, poor light-curve sampling (i.e., for MB07192) can result in a lack of a microlensing parallax signal from the light curve alone, even for long-timescale events. Second, the mass–distance relation that results from a direct measurement of $\pi_{\rm E}$ (via lens–source separation) allows for the "continuous degeneracy" to be completely broken.

Although the host mass and lens system distance have now been precisely measured as a result of the direct detection in HST and Keck, the sampling of the light-curve photometry during the microlensing event remains poor. This means that the large uncertainty in the mass-ratio parameter (q in Table 6) results in a large error in the inferred mass of the planetary companion ($m_{\rm p}$ in Table 7). As previously mentioned in Section 2, the large uncertainty in the planetary companion mass comes from a combination of factors: the event is located in a MOA field with a relatively low cadence, which leads to poor sampling of the light curve, and the planetary signal was not detected in real time. It was several days after the photometric peak that the anomaly in the light curve was alerted.

In conclusion, the distance to the MB07192 lens system is ∼3× larger than previously reported, now at a distance of approximately 2 kpc. Both the mass of the host star and planetary companion are also 2–5× larger than previously

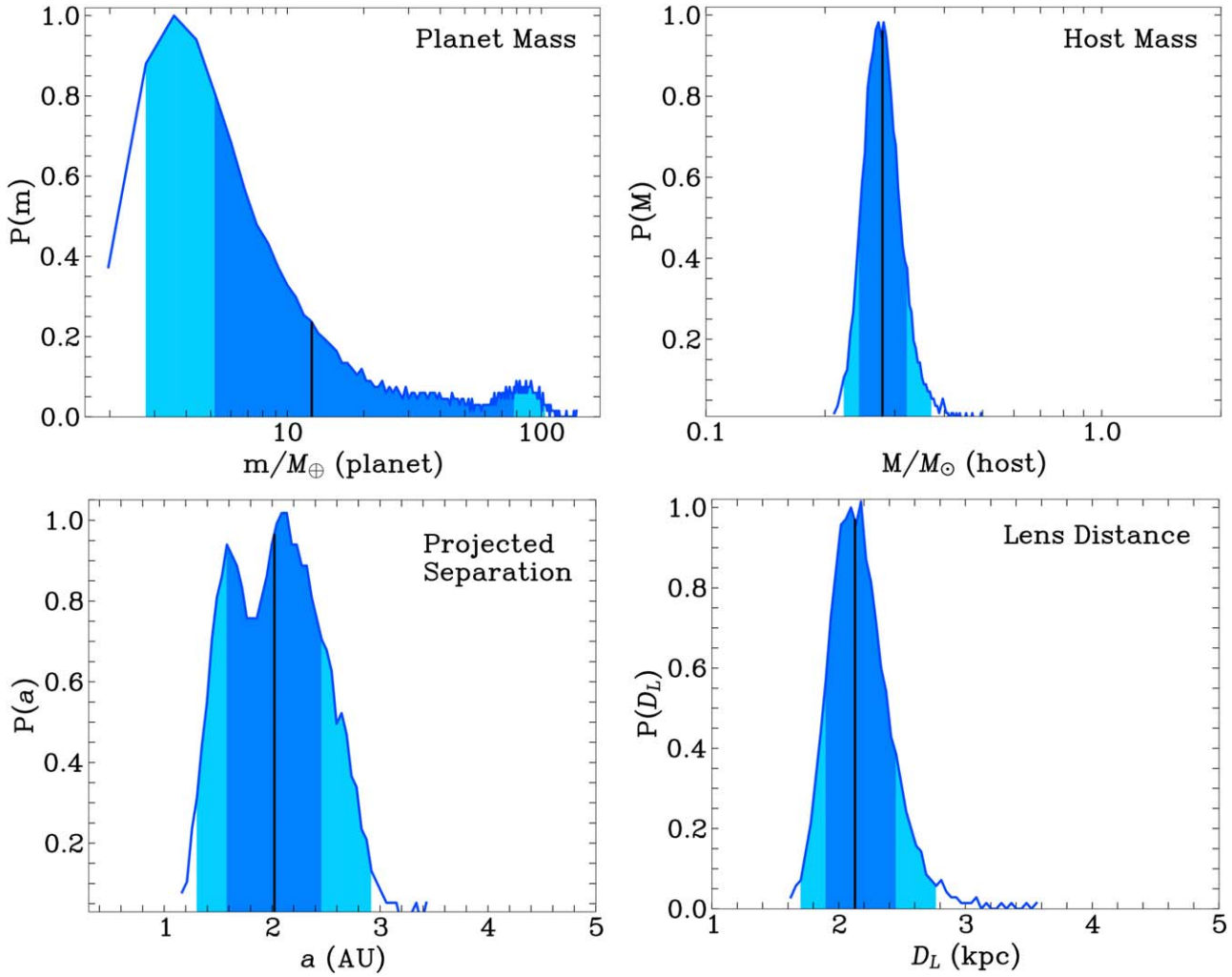

Figure 8. The posterior probability distributions for the lens system physical parameters: planetary companion mass (upper left), host mass (upper right), 2D projected separation (lower left), and lens distance (lower right). The vertical black line shows the median of the probability distribution for each parameter. The central 68% of each distributions is shown in dark blue, with the remaining central 95% shown in light blue.

reported, which now extends the possible mass range for the planet to a possible sub-Saturn-class planet. However, as the top-left panel of Figure 8 shows, the most likely mass for the planetary companion remains in the super-Earth range ($\sim$3–12 $M_\oplus$). Previous studies reported a smaller planet mass and also underestimated the error bars on the planet mass for several reasons. All of the B08 models report a too large microlensing parallax value, which led to a smaller derived planet mass compared to the median value of the planet mass that we report here. Further, the B08 and K12 caustic-crossing models contributed significant weighting to the combined results, which gave much smaller error bars on the derived planet mass. Our new results have ruled out the caustic-crossing models, which now gives larger error bars on the derived planet mass, particularly the upper 1σ error.

The results of this work have several implications for the upcoming RGES. If Roman is expected to employ lens flux measurement methods similar to those described in this work, then a careful selection of secondary observing filters must be made to avoid or minimize instances of the "continuous degeneracy." For example, the mass–luminosity relation given by a bluer Roman passband would have a smaller overlap with the mass–distance relation given by θ_E compared to other redder Roman filters. This effect is more severe for nearby M-dwarf lenses (i.e., Figure 7). Also, for Roman detected events with very faint sources or very short Einstein timescales that do not have a measurable microlensing parallax signal, a successful lens–source flux measurement by Roman itself will be important for breaking possible degeneracies like those discussed in this work.

Acknowledgments

The authors would like to thank the anonymous referee for helpful comments that improved the structure and led to a stronger manuscript. This paper is based in part on observations made with the NASA/ESA Hubble Space Telescope, which is operated by the Association of Universities for Research in Astronomy, Inc., under NASA contract NAS 5-26555. The Keck Telescope observations and data analysis were supported by a NASA Keck PI Data Award, grant No. 80NSSC18K0793, administered by the NASA Exoplanet Science Institute. All of the HST data used in this paper can be found in MAST: 10.17909/wbe0-3a21. Data presented herein were obtained at the W. M. Keck Observatory from telescope time allocated to the National Aeronautics and Space Administration through the agency's scientific partnership with the California

Institute of Technology and the University of California. The Observatory was made possible by the generous financial support of the W. M. Keck Foundation. The authors wish to recognize and acknowledge the very significant cultural role and reverence that the summit of Maunakea has always had within the indigenous Hawaiian community. We are most fortunate to have the opportunity to conduct observations from this mountain. The material presented here is also based upon work supported by NASA under grant No. 80GSFC21M0002. This work was supported by the University of Tasmania through the UTAS Foundation and the endowed Warren Chair in Astronomy and the ANR COLD-WORLDS (grant No. ANR-18-CE31-0002). Part of this work was authored by employees of Caltech/IPAC under Contract No. 80GSFC 21R0032 with the National Aeronautics and Space Administration. Lastly, portions of this research were supported by the Australian Government through an Australian Research Council Discovery Program (project No. 200101909) grant awarded to A.C. and J.P.B.

Software: `DAOPHOT-II` (Stetson 1987), daophot _ mcmc (Terry et al. 2021), eesunhong (Bennett & Rhie 1996), emcee (Foreman-Mackey et al. 2013), genulens (Koshimoto & Ranc 2021), hst1pass (Anderson 2022), KAI (Lu 2022), Matplotlib (Hunter 2007), Numpy (Oliphant 2006), Spyctres (Bachelet 2024), SWarp (Bertin 2010).

Appendix A
2023 Hubble Space Telescope Snapshot Images

Figure 9 shows the four-panel figure created from the two exposures taken during the 2023 August Snapshot Program (Sahu et al. 2023). The stacked frame has noticeably larger Poisson noise than the previous HST epochs, which have 4× more exposures. The longer time baseline between the peak of the microlensing event and the 2023 HST data helps to mitigate the lack of exposures, as the larger separation between source and lens can be clearly detected in this epoch.

These 2023 data, in conjunction with the previous HST epochs, largely confirm that the two stars we detect are the true source and lens separating from each other with their expected relative proper motions. This multiepoch tracking rules out the scenarios in which we are detecting an unrelated blend or a bound stellar companion to either the source or lens.

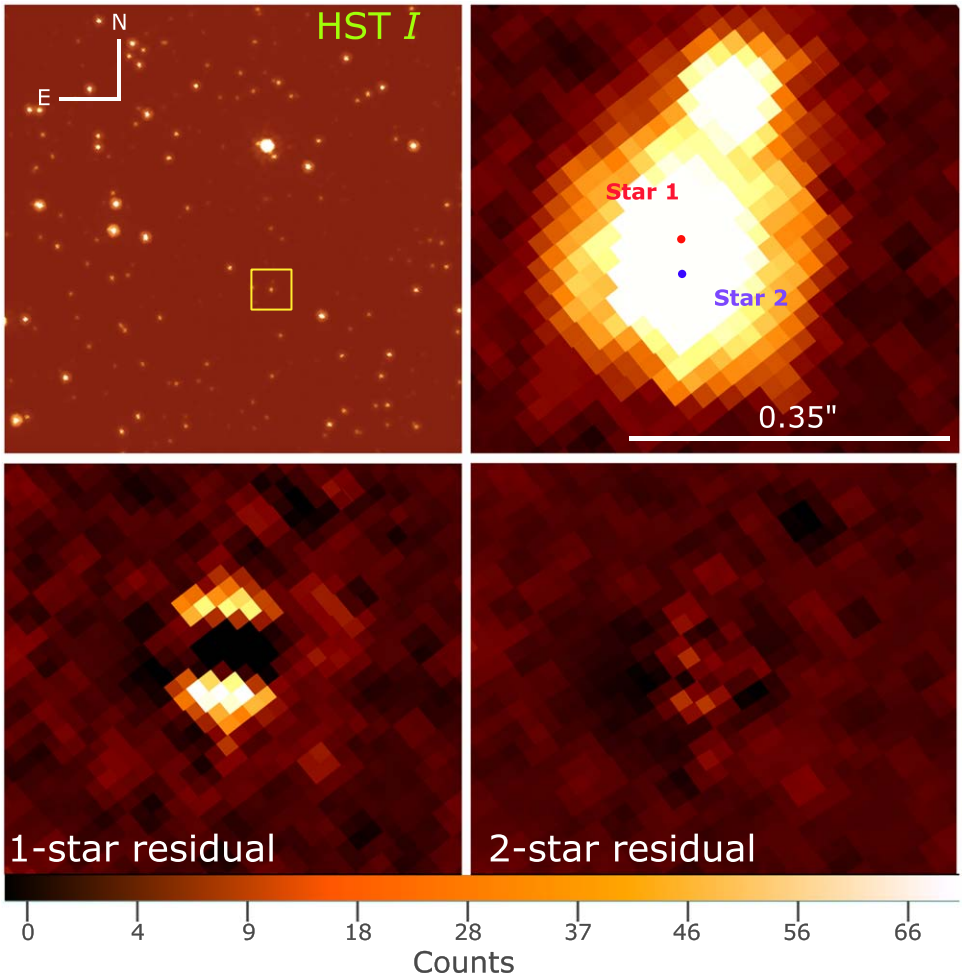

Figure 9. Top left: the 2023 HST *I*-band stack image created from two individual exposures from the Snapshot Program. The target is indicated with a yellow box. Top right: zoomed image of the target, with the two points indicating the best-fit positions for the two stars from the multi-star PSF fitting. We note the unrelated neighbor star has moved closer to the target(s) by ∼1 pixel between the 2012 and 2023 HST data. Bottom left: the residual image from a single-star PSF fit, showing a strong signal of the blended lens (source). Bottom right: residual image for the simultaneous two-star PSF fit, showing a smoother subtraction with Poisson noise remaining as well as systematics due to the less characterized PSF model. The color bar represents the pixel intensity (counts) seen in the top-right and bottom-left/bottom-right panels.

Appendix B
Full Light-curve Modeling Comparison

We show in Figure 10 a comparison of the fitting parameters between the light-curve modeling from photometry only and from photometry plus HST/Keck AO imaging. In Sections 3 and 5, we explained one of the strongest high-resolution imaging constraints is that of the microlensing parallax vectors, particularly the north component, $\pi_{\rm E,N}$. Additionally, the tighter constraint on the source radius crossing time, t_*, comes primarily from the $\mu_{\rm rel,H}$ measurement derived from the Keck data via the following equation:

$$t_* = \frac{\theta_*}{\mu_{\rm rel}}, \tag{B1}$$

where θ_* is the angular size of the source star, which we estimate using surface brightness relations from Boyajian et al. (2014),

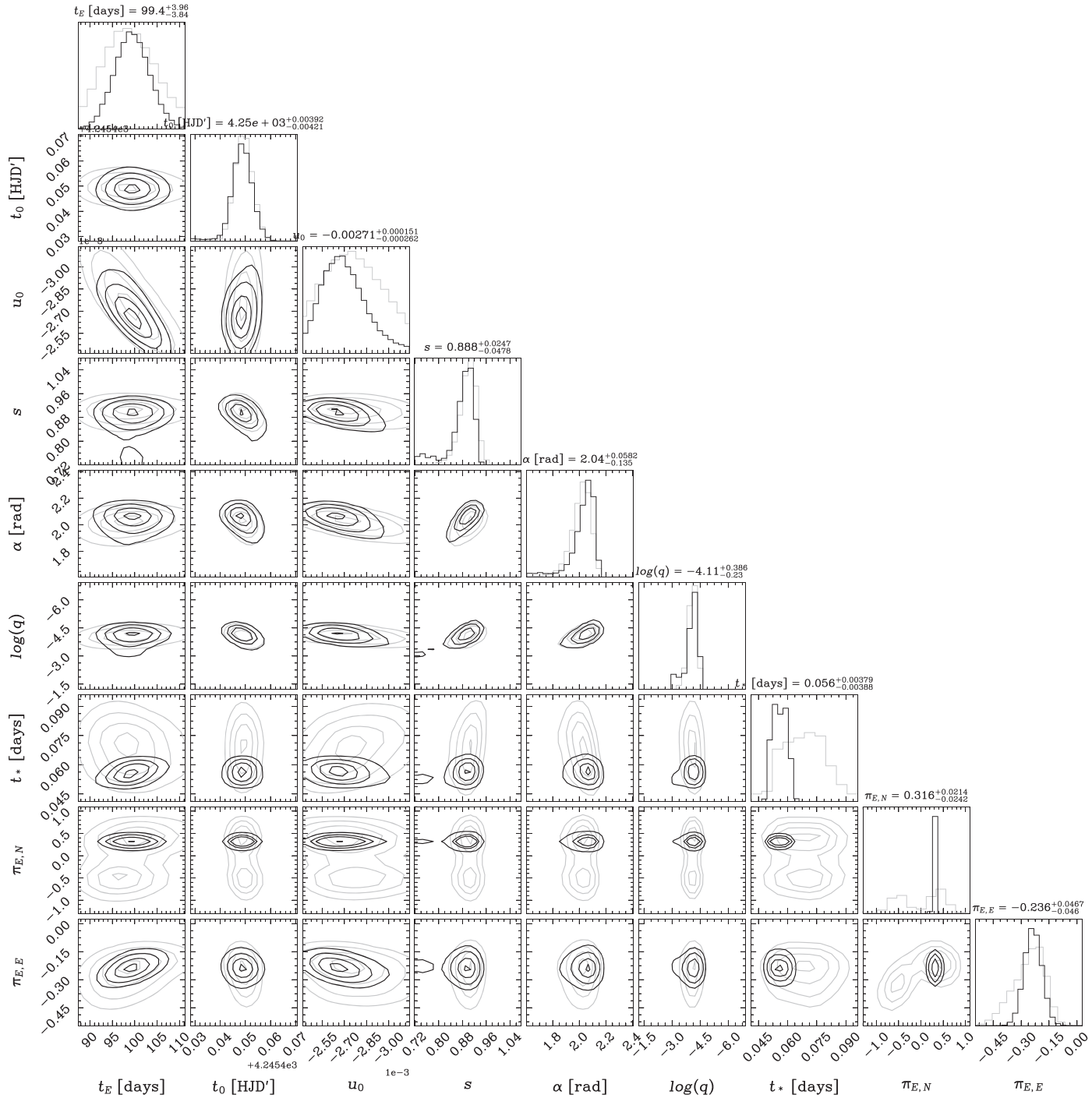

Figure 10. Comparison of model parameter distributions from the light-curve photometry only (light gray) and light-curve photometry plus HST/Keck imaging constraints (black). The two cases shown are for the $s < 1$, $u_0 < 0$ model. The constraints from the high-resolution imaging are tightened most for the north and east components of the microlensing parallax ($\pi_{\rm E,N}$, $\pi_{\rm E,E}$) as well as the source radius crossing time (t_*). The median values given in the title headings (above each histogram) are for the constrained light curve and imaging model. All other model parameters give consistent distributions between the two cases.

considering only stars spanning the range in colors that are relevant for microlensing targets. This yields an angular source size of $\theta_* = 0.47 \pm 0.09\,\mu$as for this target. The value of $\mu_{\rm rel}$ in Equation (B1) comes from the best-fit lens–source separation measurement in Keck.

As described in Section 5, the caustic-crossing models are largely ruled out, and the models with a close approach to a caustic cusp do not strongly constrain t_* very well. Ultimately, we can further reduce the total number of possible solutions from K12 (eight solutions) by a factor of 2, which leaves a fourfold degeneracy remaining (i.e., $s \rightarrow 1/s$ and $u_0 < 0$, $u_0 > 0$).

Appendix C
Spectral Energy Distribution Fitting

Using the direct V-, I-, and K-band magnitude measurements for both the source and the lens stars, it is possible to perform a spectral energy distribution fit for these two objects. We used the `Spyctres` software (Bachelet 2024) to model the stars' fluxes, parameterized with θ_*, $T_{\rm eff}$, [Fe/H], and $\log(g)$. The spectra template were generated with the Kurucz (1993) models and the extinction is modeled using the absorption laws from Wang & Chen (2019), which use only A_V as a free parameter. We note that the absorption toward the lens has been parameterized with $\epsilon = A_{V_L}/A_{V_S}$. We use a Gaussian prior on the source extinction A_V from Table 3. The posterior distribution was explored with the MCMC algorithm implemented in `emcee` (Foreman-Mackey et al. 2013). As can be seen in Figure 11, the best models replicate the observations accurately. Lastly, the angular source radius modeled with `Spyctres` ($\theta_* = 0.49 \pm 0.04\,\mu$as) is in excellent agreement with our earlier estimation based on Boyajian et al. (2014; $\theta_* = 0.47 \pm 0.09\,\mu$as).

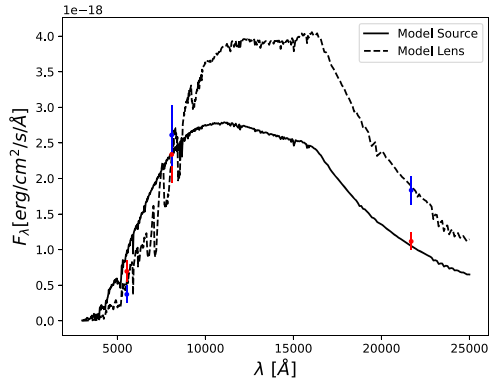

Figure 11. Spectral energy distribution measurements for the source (red) and lens (blue) for MB07192 in the V, I, and K bands. The model spectra for the source star (solid line) and lens star (dashed line) are from Kurucz et al. (1993) while the absorption law of Wang et al. (2019) is adopted.

Appendix D
Near-infrared Color–Magnitude Diagram

Figure 12 shows the $(J-H, H)$ near-IR CMD for the MB07192 field. Similar to Figure 4, the HST CMD of all detected sources from the 2012 epoch is shown in green, with OGLE-III stars cross-identified in the VVV catalog shown in red. Although there is no direct identification of the lens in the HST J -and H-band data, we estimate the lens magnitude via the excess flux (e.g., blend) that is

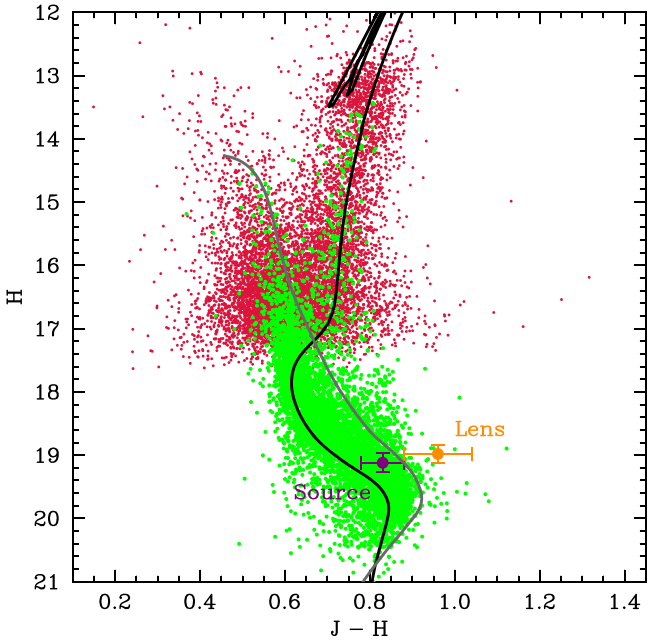

Figure 12. Similar to Figure 4, but for the HST near-IR passbands (F125W − J band, F160W − H band). The purple and orange points indicate the inferred source and lens colors and magnitudes, respectively, with associated uncertainties. MIST isochrones for the observed bulge population (black curve) and foreground disk population (gray curve) are shown.

measured on top of the source star in these two passbands. The lens star is estimated to be $(J-H)_L, H_L = (0.98 \pm 0.08, 18.91 \pm 0.15)$, and the source star is $(J-H)_S, H_S = (0.83 \pm 0.05, 19.12 \pm 0.14)$. These estimates are consistent with the source/lens magnitude directly measured in the other passbands (HST V and I, Keck K), considering the $E(J-K)$ reddening, A_J and A_H extinctions (Table 3).

Lastly, we show two near-IR isochrones with subsolar metallicity from the MESA Isochrones & Stellar Tracks (MIST) database (Paxton et al. 2015; Dotter 2016; Choi et al. 2016). This includes stars approximately 10 Gyr in age, with metallicity [Fe/H] = −0.25 and mass fraction $[Z] = 0.01$. The isochrone given by the black curve is well fit to the observed (background) bulge population of stars in the field, and the isochrone given by the gray curve is well fit to the observed (foreground) disk population of stars. As previously mentioned, we deduce the lens is likely an M4 dwarf in the disk at a distance of ∼2 kpc. The source is likely a G-type main-sequence star in the Galactic bulge at a distance of ∼7 kpc.

ORCID iDs

Sean K. Terry https://orcid.org/0000-0002-5029-3257
Jean-Philippe Beaulieu https://orcid.org/0000-0003-0014-3354
David P. Bennett https://orcid.org/0000-0001-8043-8413
Andrew A. Cole https://orcid.org/0000-0003-0303-3855
Naoki Koshimoto https://orcid.org/0000-0003-2302-9562
Jay Anderson https://orcid.org/0000-0003-2861-3995
Etienne Bachelet https://orcid.org/0000-0002-6578-5078
Joshua W. Blackman https://orcid.org/0000-0001-5860-1157
Ian A. Bond https://orcid.org/0000-0002-8131-8891
Jessica R. Lu https://orcid.org/0000-0001-9611-0009
Jean Baptiste Marquette https://orcid.org/0000-0002-7901-7213

Clément Ranc https://orcid.org/0000-0003-2388-4534
Natalia E. Rektsini https://orcid.org/0000-0002-1530-4870
Kailash Sahu https://orcid.org/0000-0001-6008-1955
Aikaterini Vandorou https://orcid.org/0000-0002-9881-4760

References

Alcock, C., Allsman, R., Axelrod, T., et al. 1996, ApJ, 461, 84
Anderson, J. 2022, Instrument Science Report WFC3 WFC3 2022-5
Anderson, J., & King, I. R. 2006, ACS Instrument Science Report 2006–01
Bachelet 2024, ebachelet/Spyctres, v0.4.2, Zenodo, doi:10.5281/zenodo.10999075
Beaulieu, J. P., Batista, V., Bennett, D. P., et al. 2018, AJ, 155, 78
Bennett, D. 2018, Keck Observatory Archive N139
Bennett, D., Sumi, T., Bond, I., et al. 2012a, ApJ, 757, 119
Bennett, D. P. 2008, Exoplanets (Berlin: Springer), 47
Bennett, D. P. 2010, ApJ, 716, 1408
Bennett, D. P., Anderson, J., Bond, I. A., Udalski, A., & Gould, A. 2006, ApJL, 647, L171
Bennett, D. P., Anderson, J., & Gaudi, B. S. 2007, ApJ, 660, 781
Bennett, D. P., Bhattacharya, A., Anderson, J., et al. 2015, ApJ, 808, 169
Bennett, D. P., Bhattacharya, A., Beaulieu, J.-P., et al. 2020, AJ, 159, 68
Bennett, D. P., Bhattacharya, A., Beaulieu, J.-P., et al. 2024, AJ, 168, 15
Bennett, D. P., Bond, I. A., Udalski, A., et al. 2008, ApJ, 684, 663
Bennett, D. P., & Rhie, S. H. 1996, ApJ, 472, 660
Bennett, D. P., & Rhie, S. H. 2002, ApJ, 574, 985
Bennett, D. P., Rhie, S. H., Nikolaev, S., et al. 2010, ApJ, 713, 837
Bennett, D. P., Udalski, A., Bond, I. A., et al. 2018, AJ, 156, 113
Bennett, D. P. 2012b, HST Proposal GO-12541
Bennett, D. P. 2014, HST Proposal GO-13417
Bertin, E., 2010 SWarp: Resampling and Co-adding FITS Images Together, Astrophysics Source Code Library, ascl:1010.068
Bertin, E., & Arnouts, S. 1996, A&AS, 117, 393
Bhattacharya, A., Beaulieu, J. P., Bennett, D. P., et al. 2018, AJ, 156, 289
Bhattacharya, A., Bennett, D. P., Beaulieu, J. P., et al. 2021, AJ, 162, 60
Blackman, J. W., Beaulieu, J. P., Bennett, D. P., et al. 2021, Natur, 598, 272
Bond, I. A., Abe, F., Dodd, R. J., et al. 2001, MNRAS, 327, 868
Bond, I. A., Bennett, D. P., Sumi, T., et al. 2017, MNRAS, 469, 2434
Boyajian, T. S., van Belle, G., & von Braun, K. 2014, AJ, 147, 47
Choi, J., Dotter, A., Conroy, C., et al. 2016, ApJ, 823, 102
Delfosse, X., Forveille, T., Ségransan, D., et al. 2000, A&A, 364, 217
Devillard, N. 1997, Msngr, 87, 19
Diolaiti, E., Bendinelli, O., Bonaccini, D., et al. 2000, A&AS, 147, 335
Dolphin, A. E., 2016 DOLPHOT: Stellar photometry, Astrophysics Source Code Library, ascl:1608.013
Dong, S., Gould, A., Udalski, A., et al. 2009, ApJ, 695, 970
Dotter, A. 2016, ApJS, 222, 8
Foreman-Mackey, D., Hogg, D. W., Lang, D., & Goodman, J. 2013, PASP, 125, 306
Gaudi, B. S. 2012, ARA&A, 50, 411
Gaudi, B. S. 2022, BAAS, 54, 102.146
Ghez, A. M., Salim, S., Weinberg, N. N., et al. 2008, ApJ, 689, 1044
Gould, A. 2022, arXiv:2209.12501
Gould, A., Dong, S., Bennett, D. P., et al. 2010, ApJ, 710, 1800
Henry, T. J., Franz, O. G., Wasserman, L. H., et al. 1999, ApJ, 512, 864
Henry, T. J., & McCarthy, D. W. J. 1993, AJ, 106, 773
Hunter, J. D. 2007, CSE, 9, 90
Ida, S., & Lin, D. N. C. 2004, ApJ, 604, 388
Johnson, S. A., Penny, M., Gaudi, B. S., et al. 2020, AJ, 160, 123
Kim, S.-L., Lee, C.-U., Park, B.-G., et al. 2016, JKAS, 49, 37
Koshimoto, N., Baba, J., & Bennett, D. P. 2021, ApJ, 917, 78
Koshimoto, N., & Ranc, C. 2021, genulens: A Tool for Gravitational Microlensing Events Simulation, v1.1, Zenodo, doi:10.5281/zenodo.4898012
Kubas, D., Beaulieu, J., Bennett, D., et al. 2012, A&A, 540, A78
Kurucz, R. L. 1993, SYNTHE Spectrum Synthesis Programs and Line Data (Cambridge, MA: Smithsonian Astrophysical Observatory)
Lissauer, J. J. 1993, ARA&A, 31, 129
Lu, J. 2022, Keck-DataReductionPipelines/KAI, v1.0.0, Zenodo, doi:10.5281/zenodo.6522913
Lu, J., Ghez, A., Hornstein, S. D., et al. 2008, ApJ, 690, 1463
Minniti, D., Lucas, P. W., Emerson, J. P., et al. 2010, NewA, 15, 433
Nataf, D. M., Gould, A., Fouqué, P., et al. 2013, ApJ, 769, 88
Nishiyama, S., Tamura, M., Hatano, H., et al. 2009, ApJ, 696, 1407
Oliphant, T. E. 2006, A Guide to NumPy, Vol. 1 (USA: Trelgol Publishing)
Paxton, B., Marchant, P., Schwab, J., et al. 2015, ApJS, 220, 15
Penny, M. T., Gaudi, B. S., Kerins, E., et al. 2019, ApJS, 241, 3
Pollack, J. B., Hubickyj, O., Bodenheimer, P., et al. 1996, Icar, 124, 62
Quenouille, M. H. 1949, AOMS, 20, 355
Quenouille, M. H. 1956, Biometrika, 43, 353
Rektsini, N. E., Batista, V., & Ranc, C. 2024, AJ, 167, 145
Sahu, K., Anderson, J., & Bond, H. E. 2023, HST Proposal GO-16716
Service, M., Lu, J. R., Campbell, R., et al. 2016, PASP, 128, 095004
Spergel, D., Gehrels, N., Baltay, C., et al. 2015, arXiv:1503.03757
Stetson, P. B. 1987, PASP, 99, 191
Sumi, T., Koshimoto, N., Bennett, D. P., et al. 2023, AJ, 166, 108
Surot, F., Valenti, E., Gonzalez, O. A., et al. 2020, A&A, 644, A140
Suzuki, D., Bennett, D. P., Ida, S., et al. 2018, ApJL, 869, L34
Suzuki, D., Bennett, D. P., Sumi, T., et al. 2016, ApJ, 833, 145
Szymański, M. K., Udalski, A., Soszyński, I., et al. 2011, AcA, 61, 83
Terry, S. K., Bennett, D. P., Bhattacharya, A., et al. 2022, AJ, 164, 217
Terry, S. K., Bhattacharya, A., Bennett, D. P., et al. 2021, AJ, 161, 54
Terry, S. K., Lu, J. R., Turri, P., et al. 2023, JATIS, 9, 018003
Tierney, L., & Mira, A. 1999, Stat. Med., 18, 2507
Udalski, A., Szymanski, M., Kaluzny, J., et al. 1994, ApJ, 426, 69
Udalski, A., Szymański, M., & Szymański, G. 2015, AcA, 65, 1
Vandorou, A., Bennett, D. P., Beaulieu, J.-P., et al. 2020, AJ, 160, 121
Wang, S., & Chen, X. 2019, ApJ, 877, 116
Yelda, S., Lu, J. R., Ghez, A. M., et al. 2010, ApJ, 725, 331